Electronic Supplementary Information

Construction of Ru@WO_{3-x}-W catalyst with hydrogen spillover effect toward ampere-level hydrogen evolution in acidic solution

Hailin Ye, Yuefei Xin, Zhengjie Zhang, Shichun Cheng, Ruyi Zhang, Mingming Wang, Yuchan Zhu* and Zhandong Ren*

Hubei Key Laboratory of Agricultural Waste Resource Utilization, School of Chemical and Environmental Engineering, Wuhan Polytechnic University, Wuhan, 430023, P. R. China.

* Corresponding author:

Zhandong Ren, Professor, School of Chemical and Environmental Engineering, Wuhan Polytechnic University, Wuhan, 430023, P. R. China.

E-mail: renzhandong@163.com. Tel.: 86-27-83943956.

Yuchan Zhu, Professor, School of Chemical and Environmental Engineering, Wuhan Polytechnic University, Wuhan, 430023, P. R. China.

E-mail: zhuyuchan@163.com. Tel.: 86-27-83943956.

1. Experimental methods

1.1 Materials

Tungsten metal target (99.99%) were purchased from Goodwill Metallic Techology Co. Ltd., Beijing, China. Ruthenium trichloride ($RuCl_3$, AR), ethanol (C_2H_5OH, AR) and titanium mesh (TM, 99.999%)were purchased from Sinopharm Chemical Reagent Co. Ltd., Shanghai, China. Commercial Pt/C (40% loading, 2-5 nm Pt size) is Johnson Matthey Co. Ltd. All reagents were analytical grade and used without further purification. Argon gas (99.999%) and oxygen gas (99.9%) was purchased from Ming-Hui Company. The water (18.25 MΩ cm^{-1}) used in all experiments was prepared by passing through an ultra-pure purification system.

1.2 Preparation of W/TM

With 99.99% W as sputtering targets and Titanium mesh (TM) as the substrate, W was prepared by magnetron sputtering with DC power supply. Before sputtering, the Ti foil substrate was washed and degreasing, and installed on the sample stage of the vacuum chamber of the magnetron sputtering instrument. Before the formal sputtering, the vacuum chamber was first evacuated to 4×10^{-4} Pa, and replaced with high-purity argon repeatedly to remove the air in the vacuum chamber. Then introduce high-purity argon, adjust the pressure of the vacuum chamber to 1.0 Pa. The sputtering power is controlled at 40 W and the sputtering time is 40 min, thus obtaining W/TM.

1.3 Preparation of WO_3 /TM

With 99.99% W as sputtering targets and TM as the substrate, WO_3 was prepared by magnetron sputtering with DC power supply. Prior to the formal sputtering process, the vacuum chamber was first evacuated to a base pressure of 6×10^{-2} Torr. Then the chamber was purged with an Ar:O_2 mixture at a flow ratio of 30:30 standard cubic centimeters per minute (sccm) for 20 min and the chamber pressure was adjusted to 4.5×10^{-2} Torr. Subsequently, sputtering was then carried out at a constant current of 100 mA for a duration of 1600 s, resulting in the preparation of the WO_3/TM electrode.

1.4 Preparation of WO_{3-x}-W/TM

In order to obtain WO_{3-x}-W/TM, the W electrode prepared above was immersed in 0.5 M H_2SO_4 solution, and the cyclic voltametric (CV) scanning was carried out at 10 mV s^{-1} in the range of 1.2 ~ 2.0 V (vs. RHE) for 40 segments. In order to change the oxidation degree of W surface, the scan rate were set to 10, 20, 30, 40 and 50 mV s^{-1}, and the samples were recorded as WO_{3-x}-W/TM-S_1, WO_{3-x}-W/TM-S_2, WO_{3-x}-W/TM-S_3, WO_{3-x}-W/TM-S_4 and WO_{3-x}-W/TM-S_5。

1.5 Preparation of Ru@WO_{3-x}-W/TM、Ru@W/TM and Ru/TM

The electrodeposition experiment was carried out on CHI600e electrochemical workstation. The working electrode are WO_{3-x}-W/TM、W/TM and TM, the reference electrode is Hg/Hg_2SO_4/0.1M K_2SO_4, and the counter electrode is carbon paper electrode. The electrolyte concentration is 0.5 mM $RuCl_3$. Before electrodeposition, introduce the high-purity argon gas for 10 minutes to remove oxygen from the solution. Ru@WO_{3-x}-W/TM electrode was prepared by electrodeposition under the conditions that the scan rate was 5 mV s^{-1}, the potential range was -0.5 ~ 0.3 V (vs. RHE) and the number of segments was set to 10. The preparation process of Ru@W/TM or Ru/TM is the same as that of Ru@WO_{3-x}-W electrode, except that WO_{3-x}-W/TM is not used, and W/TM or TM is used instead. The loading of Ru and W can be determined by EDXRF, and the results are listed in Table S1 (ESI†).

1.6 Preparation of Pt/C electrode

1 mg 40 wt% Pt/C powders (Johnson Matthey) was mixed with 1 ml 0.05 wt% nafion-ethanol solution respectively to prepare catalyst ink. After ultrasonic mixing, 50 μL of Pt/C ink was added dropwise to the TM substrate (1.0 cm^2) with a loading of 50 μg cm^{-2}.

1.7 Material characterization

X-ray diffraction (XRD) patterns were acquired on an XRD-7000 X-ray diffractometer

(Shimadzu, Japan). Transmission Electron Microscopy (TEM) were conducted on an JEM-2100F (JEOL, Japan). X-ray photoelectron spectrometry (XPS: ESCLAB 250Xi, Thermo Fisher Scientific, The United States) with monochromatized Al Ka radiation was used to analyze the electronic properties. Analysis of the composition of the electrode was carried out by X-ray fluorescence (XRF: EDX-7000, Shimadzu, Japan).

1.8 Electrochemical measurements

The electrochemical experiments were carried out in a typical three-electrode electrochemical cell with a carbon paper as a counter electrode and $Hg/Hg_2SO_4/K_2SO_4$ as the reference electrode. Cyclic voltammetry (CV) measurements were performed in Ar-saturated 0.5 M H_2SO_4 solution at the scan rate of 100 mV s^{-1} in the potential of 0 ~ 1.4V. The activity of hydrogen evolution reaction (HER) was characterized by linear voltammetry scanning (LSV) in 0.5 M H_2SO_4 solution at a scanning speed of 5 mV s^{-1}. Electrochemical stability testing is to continuously test the HER activity at a fixed potential for 100 h. Electrochemical impedance spectroscopy (EIS) was recorded under the condition of frequency of 100 mHz ~ 100 kHz and ac voltage amplitude of 50 mV.

1.9 TOF calculation

The TOF is calculated from the equation:

$$TOF = (j \times S)/2 \times F \times n$$

where j, S, F, n are the measured current density, the surface area of the electrode (cm^2), the Faraday constant (1.602×10^{-19} C) and the moles of the metal atom on corresponding electrode, respectively. Here, 2 is the number of electrons to product one H_2 molecule. Note that the value of n can be achieved based on mass loading and the weight % of Ru in electrocatalysts, and the assumption of all Ru atoms are involved in electrocatalysis.

1.10 DFT calculation

DFT calculations were performed using the Vienna ab initio simulation package (VASP).[1] To model the exchange-correlation interactions, the Perdew-Burke-

Ernzerhof (PBE) for generalized gradient approximation (GGA) functional was adopted.[2] Ion-electron interactions were treated with the projector augmented wave (PAW) method, and a plane-wave energy cutoff of 450 eV ensured the convergence of the electronic wavefunctions.[3] Grimme's DFT-D3 correction scheme was implemented to account for the long-distance van der Waals interactions.[4] A Monkhorst-Pack k-point grid of 2×2×1 was employed for Brillouin zone sampling. Structural relaxations were performed until the Hellmann-Feynman forces on all atoms dropped below 0.05 eV/Å, while the electronic convergence criterion was set to 1×10^{-5} eV between consecutive self-consistent field iterations. Post-processing and data analysis were performed using the VASPKIT package.[5]

The computational hydrogen electrode (CHE) model put forward by Nørskov et al.[6] has been employed to calculate the Gibbs free energy of hydrogen adsorption (ΔG*H). For the reaction, the change in the Gibbs free energy (ΔG) can be described by the following equation:

$$\Delta G=\Delta E+\Delta ZPE-T\Delta S$$

where, ΔE represents the total free energy difference between the products and reactants, which can be directly obtained from DFT calculations. ΔZPE and ΔS are the zero-point energy correction and entropy change, respectively,

References

1. G. Kresse, J. Furthmüller, *Comp. Mater. Sci.* 1996, 6, 15-50.
2. J. P. Perdew, K. Burke, M. Ernzerhof, *Phys. Rev. Lett.* 1996, 77, 3865.
3. P. E. Blöchl, *Phys. Rev. B* 1994, 50, 17953.
4. S. Grimme, J. Antony, S. Ehrlich, H. Krieg, *J. Chem. Phys.* 2010, 132. 154104.
5. V. Wang, N. Xu, J.-C. Liu, G. Tang, W.-T. Geng, *Comput. Phys. Commun.* 2021, 267, 108033.
6. J. K. Nørskov, J. Rossmeisl, A. Logadottir, L. Lindqvist, J. R. Kitchin, T. Bligaard, H. Jonsson, *J. Phys. Chem. B* 2004, 108, 17886-17892.

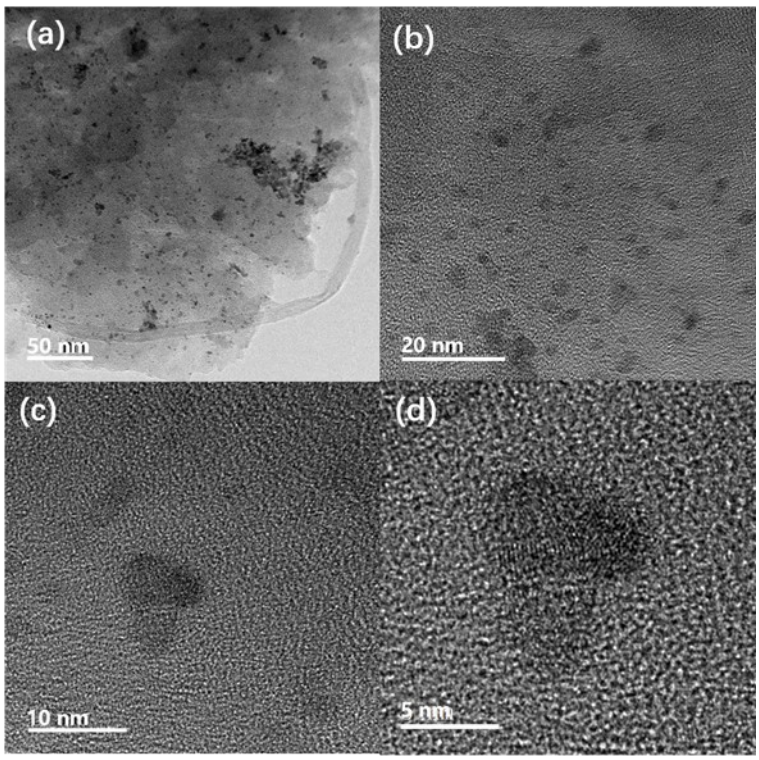

Figure S1 TEM images of Ru@WO_{3-x}-W/TM.

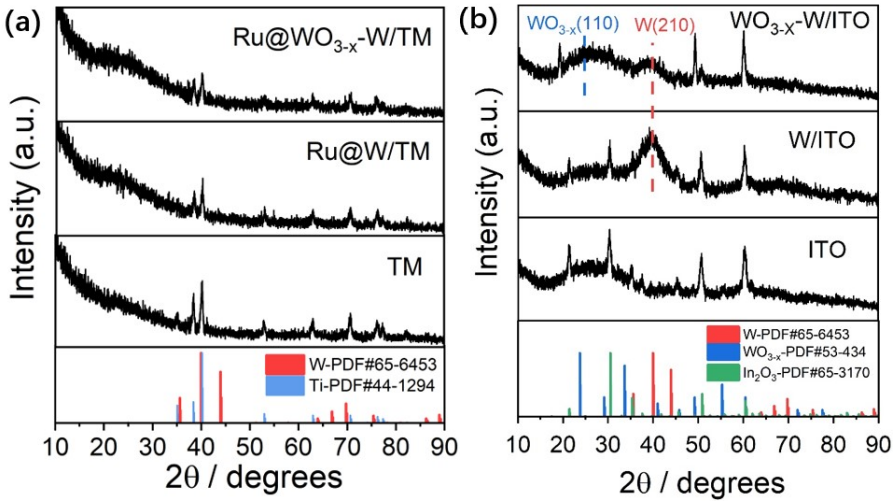

Figure S2 XRD patterns of Ru@WO_{3-x}-W/TM, Ru@W/TM and TM (a). XRD patterns of WO_{3-x}-W/ITO, W/ITO and ITO (b).

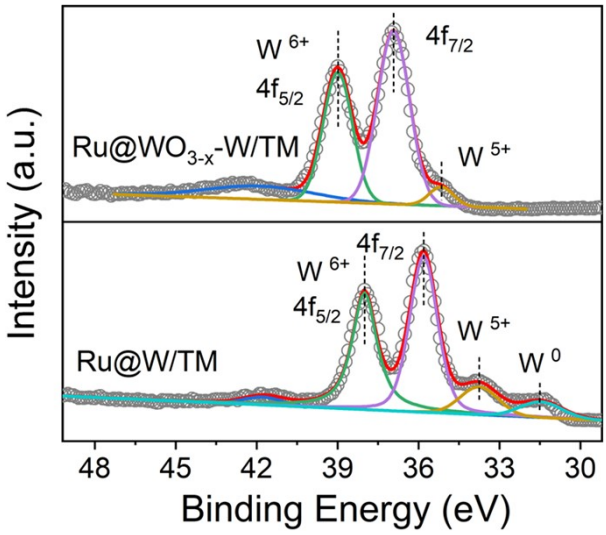

Figure S3 The W 4f spectra of Ru@WO_{3-x}-W/TM and Ru@W/TM.

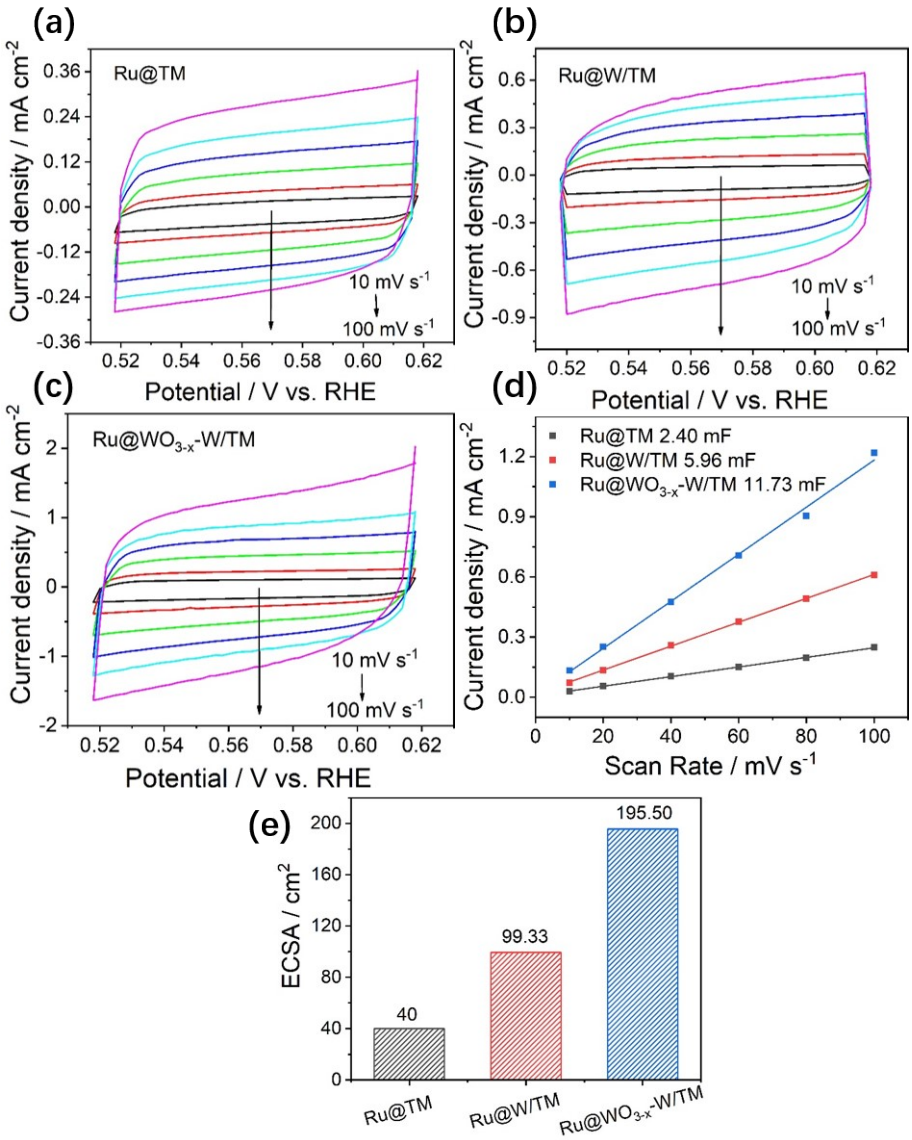

Figure S4 The double layer currents of Ru/TM (a), Ru@W/TM (b) and Ru@WO_{3-x}-W/TM (c) electrodes at different scan rates in 0.5 M H_2SO_4 solution. The double-layer capacitances (d) and ECSAs (e) of Ru/TM, Ru@W/TM and Ru@WO_{3-x}-W/TM.

It is generally believed that the increase of electrochemical surface area (ECSA) is one of the reasons for the improvement of electrochemical activity of electrode materials. The ECSAs of Ru/TM (40.0 cm^2), Ru@W/TM (99.3 cm^2) and Ru@WO_{3-x}-W/TM (195.5 cm^2) were obtained by integrating double-layer capacitors in Fig. S4 (ESI†). Obviously, the ECSA of Ru@WO_{3-x}-W/TM is the largest, which will be beneficial to improve HER activity.

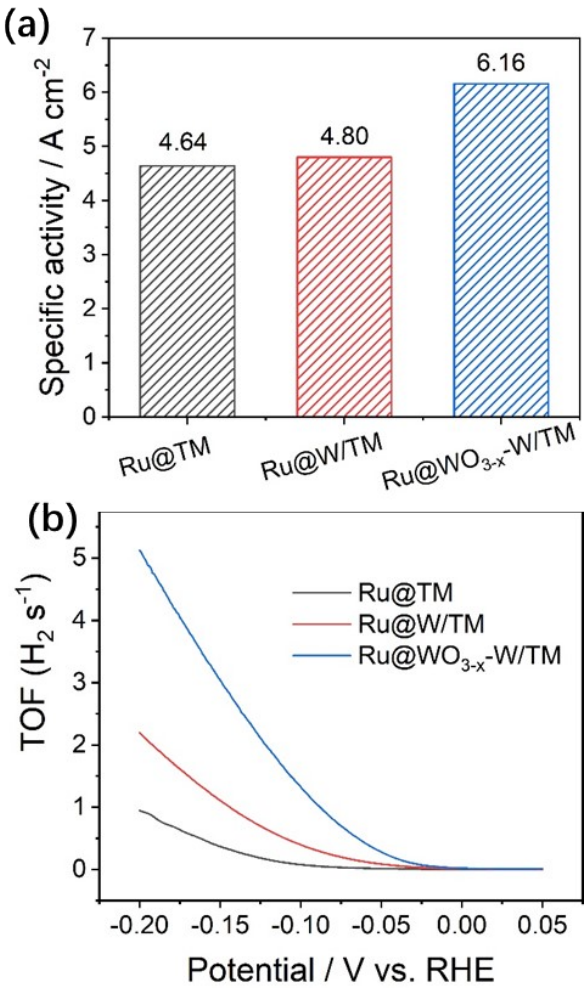

Figure S5 The SAs (a) and TOFs (b) of Ru/TM (a), Ru@W/TM (b) and Ru@WO_{3-x}-W/TM (c) electrodes

Specific activity (SA) can be obtained by the ECSA and apparent activity in Fig. S5 (ESI†), which represents the electrocatalytic reaction intrinsic ability on unit active site. SAs of Ru/TM and Ru@W/TM are 4.6 and 4.8 A cm^{-2}, which are relatively close, which indicates that the increase of HER activity of Ru@W/TM mainly comes from the increase of ECSA. However, for Ru@WO_{3-x}-W/TM, the SA increases to 6.2 A cm^{-2}, which indicated that the increase of HER activity was related to the increase of intrinsic activity of active site. In addition, the turnover Frequency (TOF) values of different electrodes are calculated, and the activity of Ru@WO_{3-x}-W/TM is the highest, which also suggests the improvement of intrinsic activity.

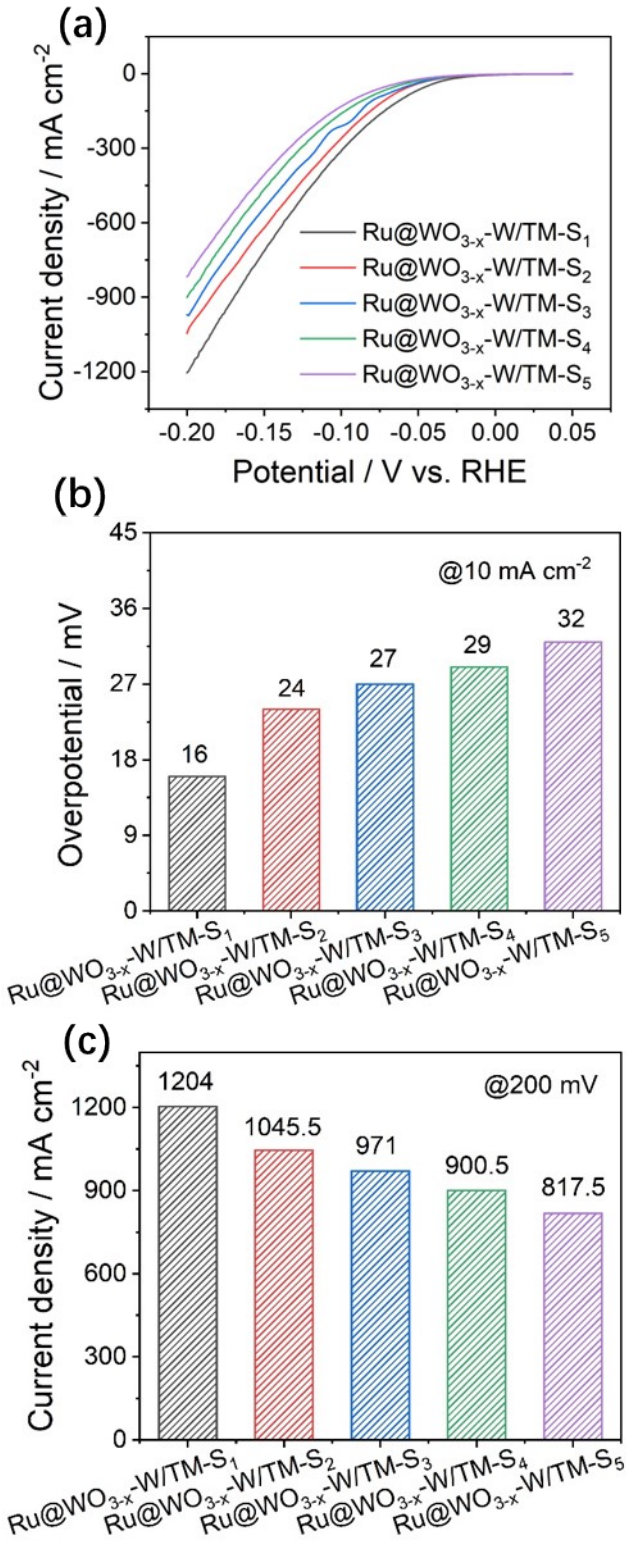

Figure S6 The LSV curves (a), η_{10} (b) and j_{200} (c) of Ru@WO_{3-x}-W/TM electrodes with different surface oxidation degrees.

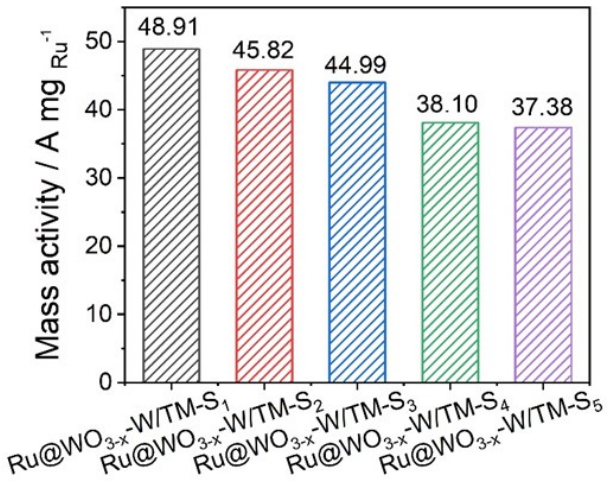

Figure S7 The MAs of Ru@WO_{3-x}-W/TM electrodes with different scan rates.

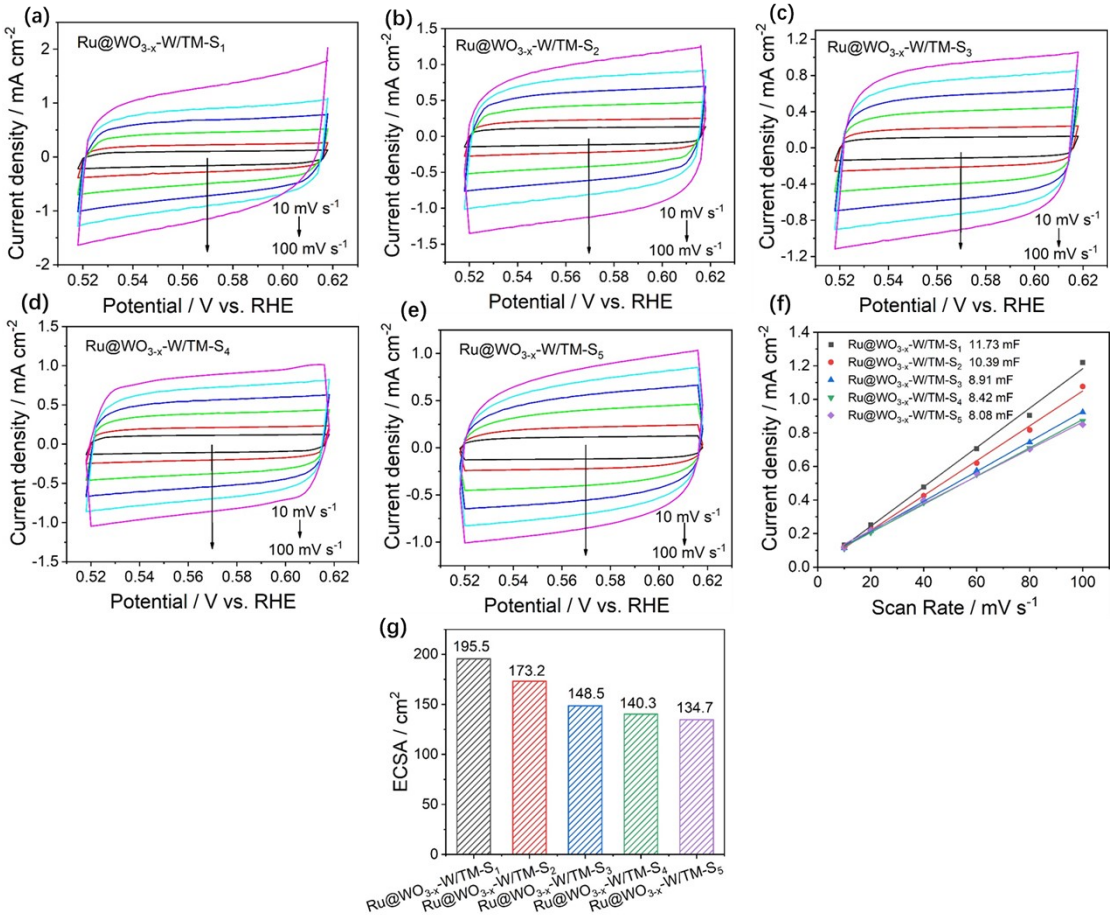

Figure S8 The double layer currents of Ru@WO_{3-x}-W/TM electrodes with different surface oxidation degrees at different scan rates in 0.5 M H_2SO_4 solution (a - e). The double-layer capacitances (f) and ECSAs (g) of Ru@WO_{3-x}-W/TM electrodes with different surface oxidation degrees.

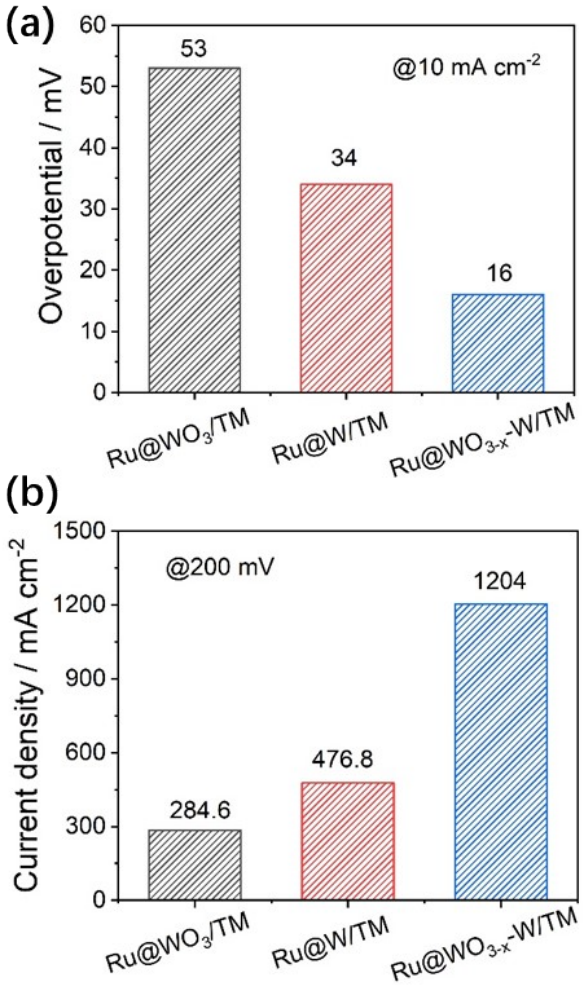

Figure S9 The η_{10} (a) and j_{200} (b) of $Ru@WO_3$/TM, Ru@W/TM and $Ru@WO_{3-x}$-W/TM.

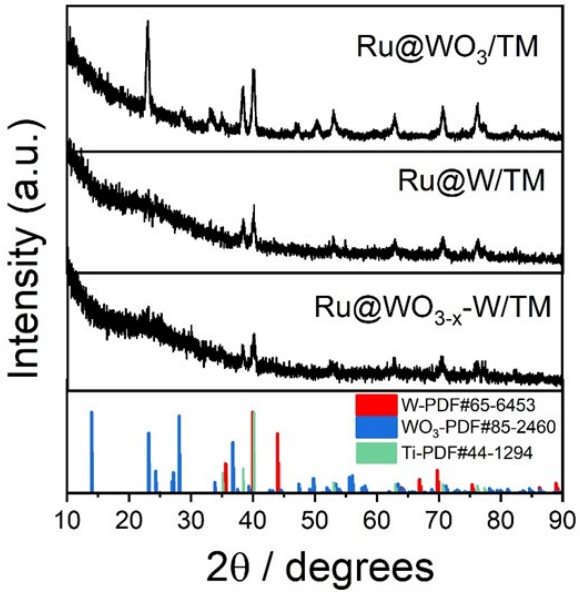

Figure S10 XRD patterns of Ru@WO_3/TM, Ru@W/TM and Ru@WO_{3-x}-W/TM.

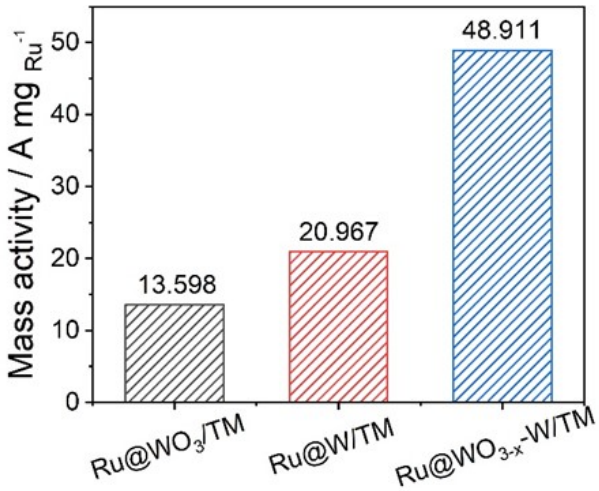

Figure S11 The MAs of $Ru@WO_3/TM$, Ru@W/TM and $Ru@WO_{3-x}$-W/TM.

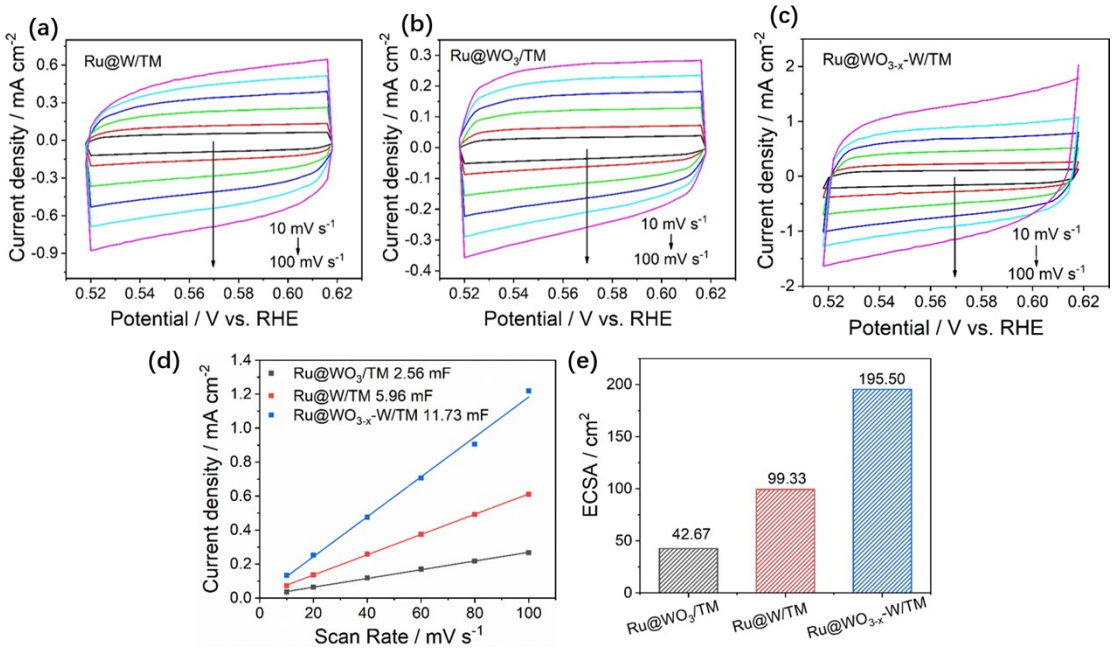

Figure S12 The double layer currents of Ru@W/TM (a), Ru@WO_3/TM (b) and Ru@WO_{3-x}-W/TM (c) at different scan rates in 0.5 M H_2SO_4 solution. The double-layer capacitances (d) and ECSAs (e) of Ru@W/TM, Ru@WO_3/TM and Ru@WO_{3-x}-W/TM.

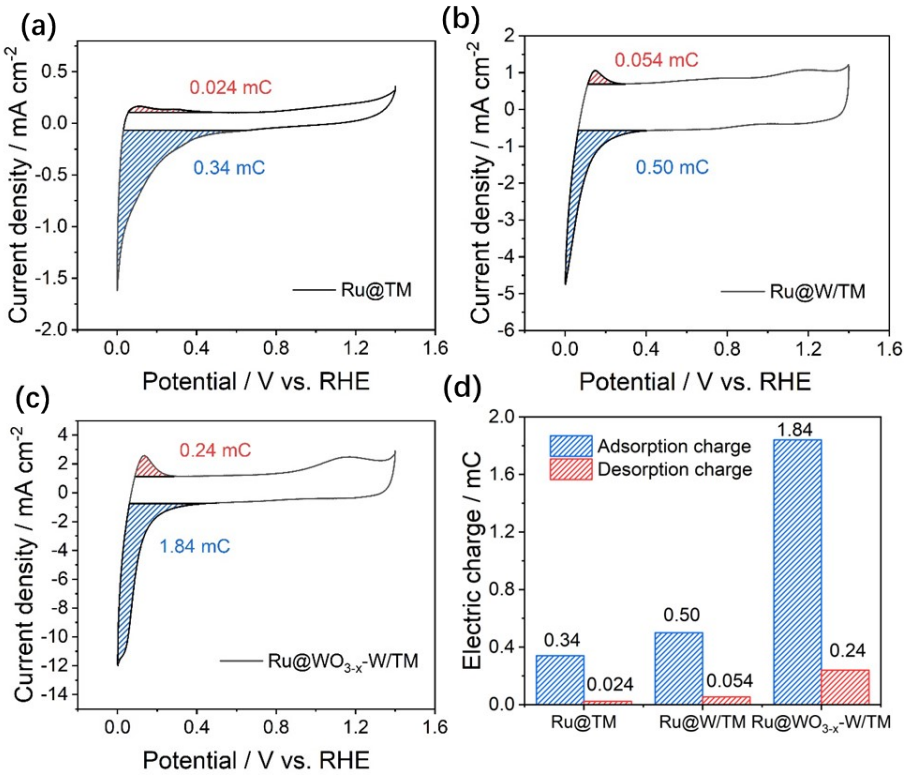

Figure S13 Charges of H adsorption and desorption of Ru/TM (a), Ru@W/TM (b) and Ru@WO_{3-x}-W/TM (c). The $q(H_{ad})$ and $q(H_{des})$of Ru/TM, Ru@W/TM and Ru@WO_{3-x}-W/TM (d).

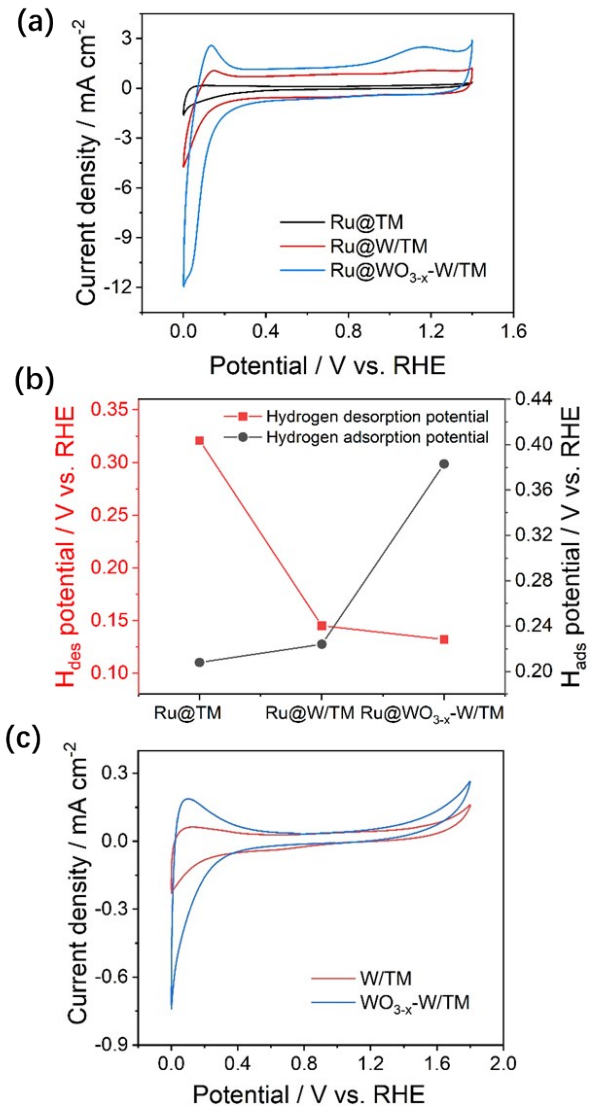

Figure S14 CV curves of Ru/TM, Ru@W/TM and Ru@WO_{3-x}-W/TM (a). The potentials of H_{ad} and H_{des} of Ru/TM, Ru@W/TM and Ru@WO_{3-x}-W/TM (b). CV curves of W/TM and WO_{3-x}-W/TM (c).

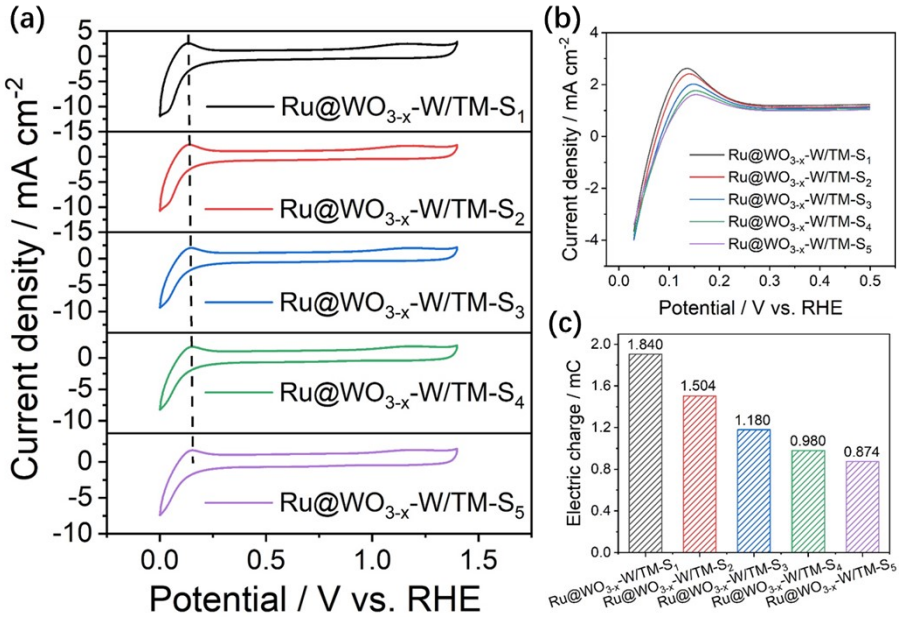

Figure S15 CV curves (a), H desorption potential (b) and H adsorption charge (c) of $Ru@WO_{3-x}$-W/TM electrodes with different surface oxidation degrees at different scan rates in 0.5 M H_2SO_4 solution.

Fig. S15a is a CV diagram of $Ru@WO_{3-x}$-W/TM electrodes with different oxidation degrees, and Fig. S15b is a comparison diagram of their hydrogen desorption curves. As can be seen from Fig. S15b, as the scan rate slows down, the surface oxidation degree increases, the formation of WO_{3-x}-W phase gradually improving, and the corresponding H desorption potential obviously decreases. Meanwhile, in Fig. S15c, with the formation of the WO_{3-x}-W phase becoming more and more complete, the adsorption capacity of H also increases obviously. These changes led to the increase of HER activity.

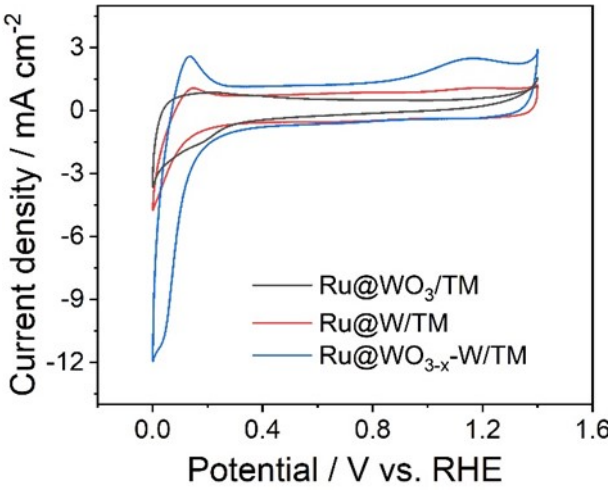

Figure S16 CV curves of $Ru@WO_3$/TM, Ru@W/TM and $Ru@WO_{3-x}$-W/TM.

It can be judged from Fig. S16 that the hydrogen adsorption potentials of $Ru@WO_{3-x}$-W/TM and $Ru@WO_3$/TM are close; However, the hydrogen desorption potentials of $Ru@WO_{3-x}$-W/TM and Ru@W/TM are close. This may indicate that WO_3 phase is favorable for adsorption, while W phase is favorable for desorption. However, $Ru@WO_{3-x}$-W/TM has both W phase and WO_3 phase, so it has favorable H adsorption/desorption characteristics.

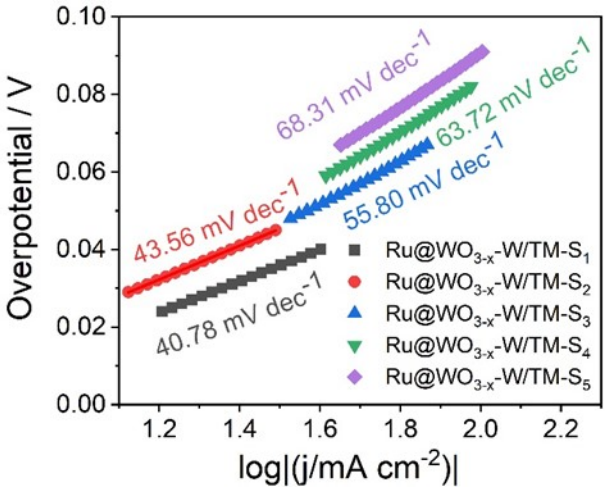

Figure S17 Tafel slopes of Ru@WO_{3-x}-W/TM electrodes with different surface oxidation degrees.

As can be seen from Fig. 17, with the gradual increase of surface oxidation degree, its Tafel slope gradually decreases, and HER kinetics continuously increases, which leads to the increase of HER activity. Their reaction mechanisms all conform to the Volmer-Heyrovsky mechanism.

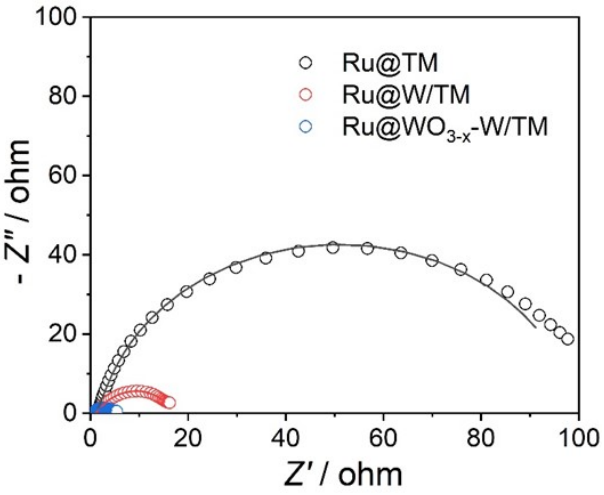

Figure S18 The EIS measurements of Ru/TM, Ru@W/TM and Ru@WO_{3-x}-W/TM at η = 50 mV.

The Nyquist diagrams of Ru/TM, Ru@W/TM and Ru@WO_{3-x}-W/TM recorded at an overpotential of 50 mV by EIS measurements in Fig. S18 (ESI†). The equivalent circuit corresponding to the EIS data is fitted with a $R_s(R_fC_f)(R_{ct}C_{dl})$ model (R_s, solution resistance; R_{ct}, charge-transfer resistance; C_{dl}, double layer capacitance). The R_{ct} of Ru@WO_{3-x}-W/TM is 2.9 Ω cm^2, while the R_{ct} values of Ru/TM and Ru@W/TM are 95.5 and 18.1 Ω cm^2. The R_{ct} of Ru@WO_{3-x}-W/TM is the lowest, suggesting fast charge transport during the HER process.

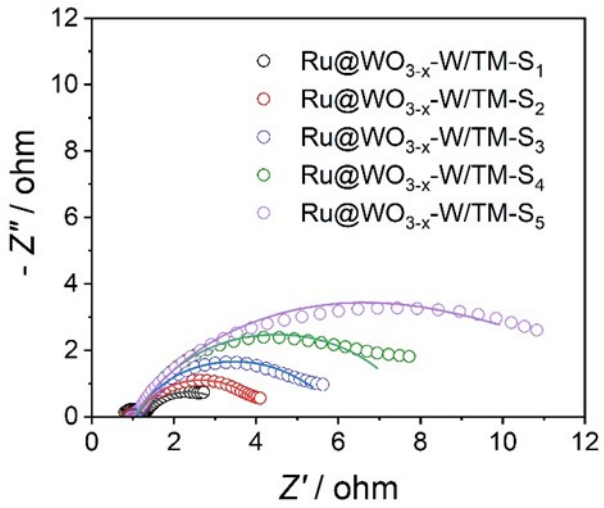

Figure S19 The EIS measurements of Ru@WO_{3-x}-W/TM electrodes with different surface oxidation degrees at η = 50 mV.

The Nyquist diagrams recorded at an overpotential of 50 mV by electrochemical impedance spectroscopy (EIS) measurements in Fig. S19 (ESI†). The R_{ct} of Ru@WO_{3-x}-W/TM electrodes with different surface oxidation degrees is 2.9, 4.1, 5.7, 7.4 and 10.1 Ω cm^2, respectively. Among them, the R_{ct} of Ru@WO_{3-x}-W/TM-S_1 electrode is the lowest, which indicates the rapid charge transfer in HER process.

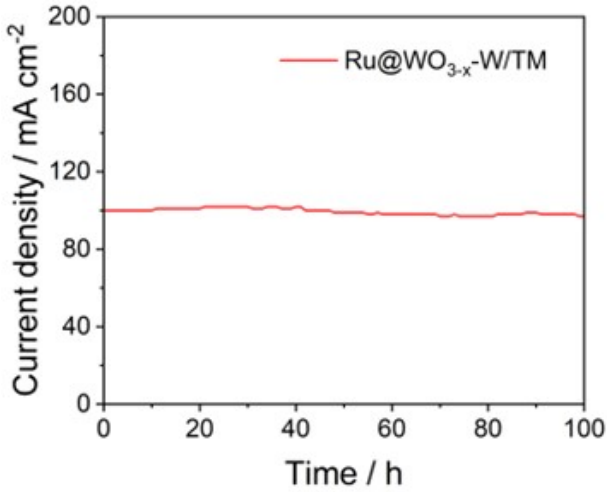

Figure S20 The long-term stability test of Ru@WO_{3-x}-W/TM at J = 100 mA cm^{-2}.

In addition, the HER activity of Ru@WO_{3-x}-W/TM is basically unchanged within 100 h at J = 100 mA cm^{-2}.

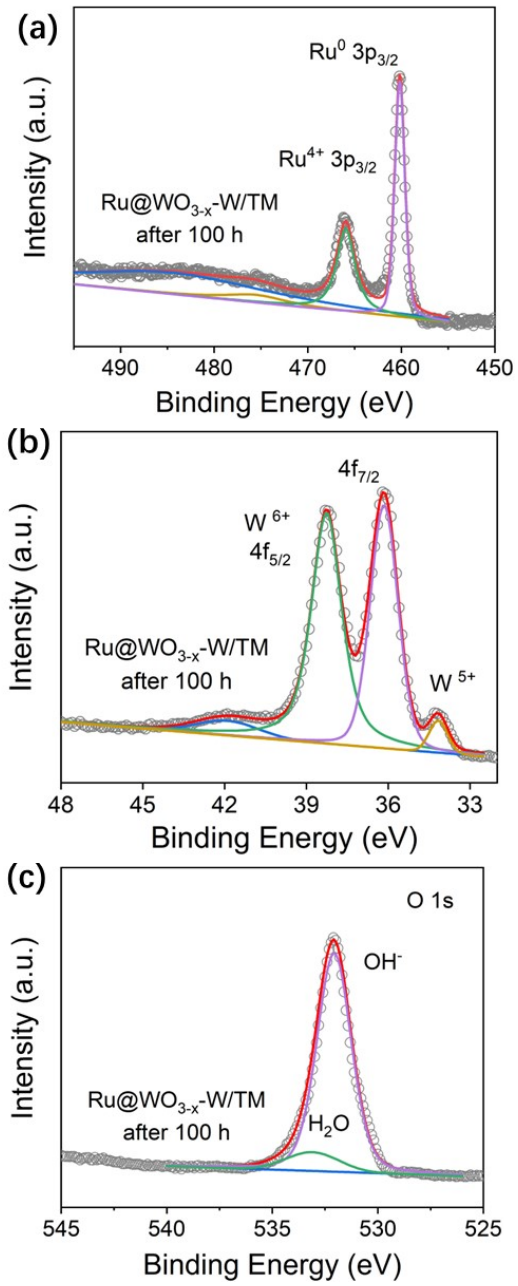

Figure S21 The Ru 3p, W 4f and O 1s spectra of $Ru@WO_{3-x}$-W/TM after 100 h.

After long-term stability testing, there was no significant change in the B.E. of Ru 3p, only a slight negative shift of 0.1 eV. At the same time, the B.E. of W 4f also showed a slight negative shift of 0.2 eV. This indicates that both Ru and W underwent slight reduction during long-term testing. But this did not affect its HER activity. There is no change in O 1s, and the B.E. peaks of OH^- and H_2O are located at 532.1 and 533.1 eV, respectively.

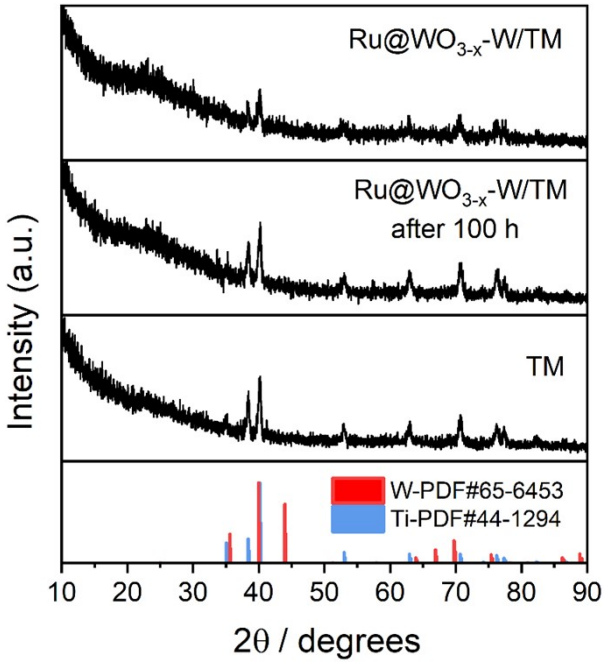

Figure S22 The XRD patterns of Ru@WO_{3-x}-W/TM and Ru@WO_{3-x}-W/TM after 100 h.

XRD analysis has shown that after long-term stability testing, there are still no observed diffraction peaks of Ru. At the same time, the Ru loading did not decrease (as evidenced by XRF analysis results), indicating that it will not agglomerate during prolonged testing.

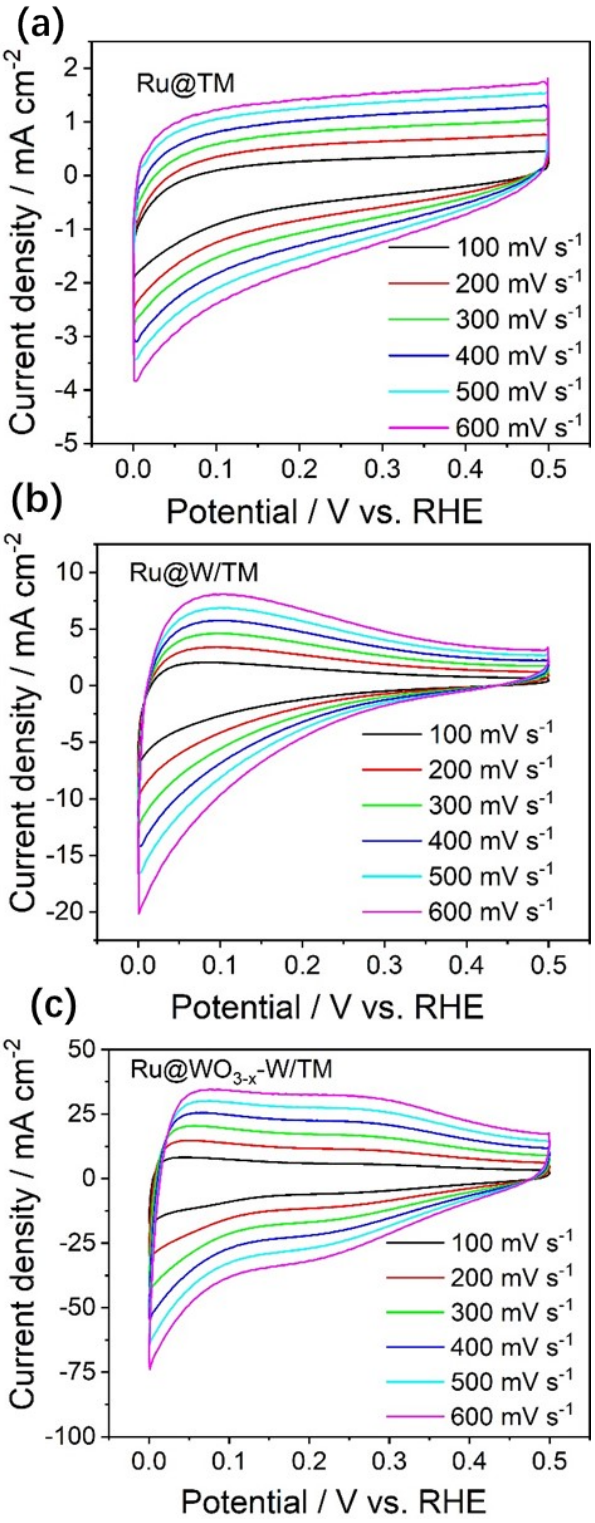

Figure S23 CV curves of Ru/TM (a), Ru@W/TM (b) and Ru@WO_{3-x}-W/TM (c) at different scan rates in the potential of 0.15 ~ 0.5 V.

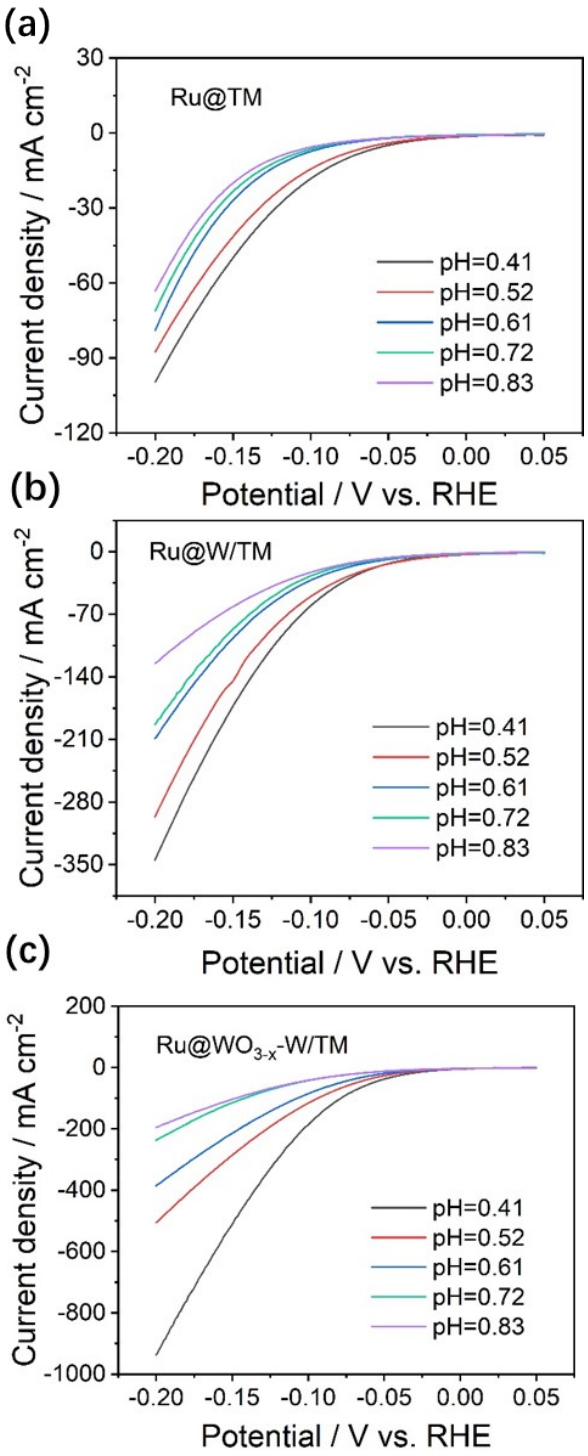

Figure S24 HER activities of Ru/TM (a), Ru@W/TM (b) and Ru@WO_{3-x}-W/TM (c) at different pH values.

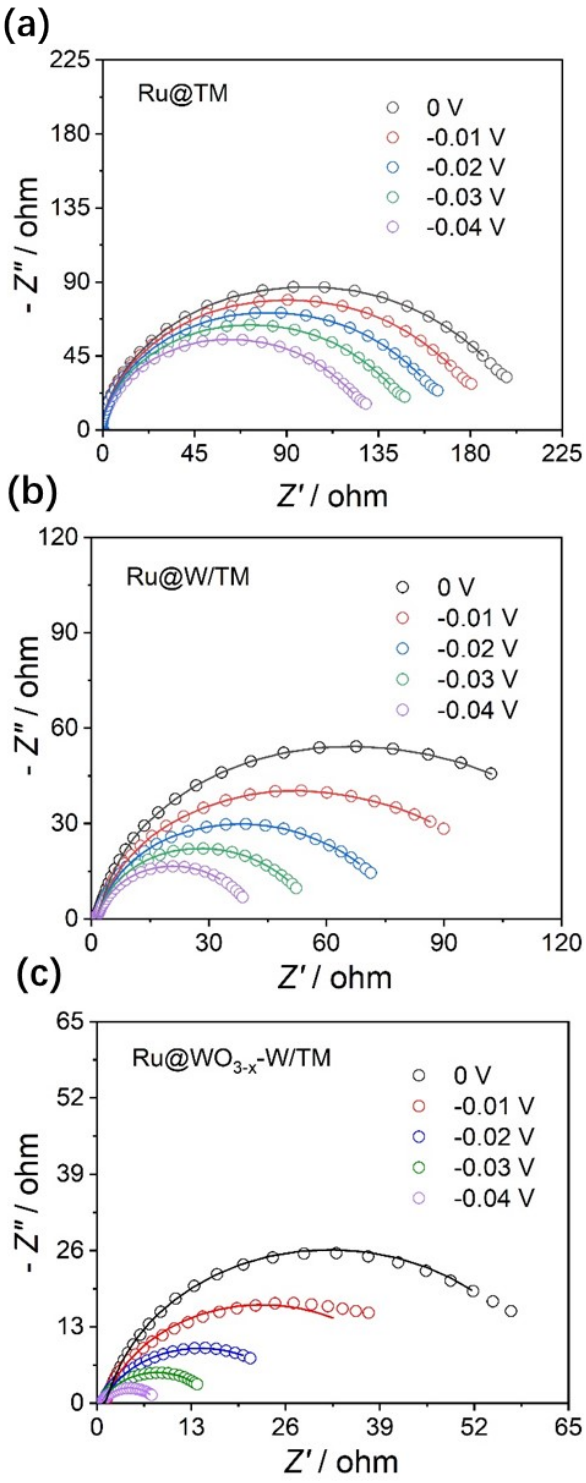

Figure S25 EIS measurements of Ru/TM (a), Ru@W/TM (b) and Ru@WO_{3-x}-W/TM (c) at different overpotential.

Table S1 Composition analysis of Ru/TM, Ru@W/TM, Ru@WO_{3-x}-W/TM, Ru@WO_3/TM and Ru@WO_{3-x}-W/TM after 100 h by EDXRF.

Electrodes	Ru Loading / μg cm^{-2}	W Loading / μg cm^{-2}
Ru/TM	20.48	-
Ru@W/TM	22.74	210.2
Ru@WO_{3-x}-W/TM	24.62	211.3
Ru@WO_3/TM	20.93	210.1
Ru@WO_{3-x}-W/TM after 100 h	21.20	217.1

Table S2 HER activities of Ru-based hydrogen spillover electrocatalyst in acidic system

No.	Catalyst	J (mA cm^{-2})	η (mV)	Tafel slope (mV/dec)	Hydrogen spillover pathway	References
1	$Al_{0.35}/Ru_{0.15}$-TCPP-CNTs	60(@ ~80 mV)	32(η_{10})	55.51	Ru→Al	Catal. Sci. Technol., 2024, 14, 735-745.
2	RuS_x/NbS_2	150(@ ~235 mV)	38(η_{10})	51.05	RuS_x→NbS_2	Angew. Chem. Int. Ed., 2024, 63, e202409465.
3	Ru/MoO_2@NCF	100(@ ~200 mV)	42(η_{10})	59.1-	MoO_2→Ru	Adv. Funct. Mater., 2024, 34, 2401452.
4	$RuSe_{1.5}$ NPs	60(@ ~75 mV)	24(η_{10})	34	Se→Ru	ACS Catal., 2024, 14, 1914-1921.
5	Ru/Ni-NiO/$Mo_2TiC_2T_x$	140(@ ~200 mV)	49(η_{10})	62	Ni-NiO→Ru	ACS Appl. Nano Mater., 2023, 6, 22192-22201.
6	$SrHf_{0.7}Ru_{0.3}O_{3-\delta}$	500(@ ~175 mV)	48(η_{10})	26	Hf→Ru	Adv. Funct. Mater., 2023, 33, 2213523.
7	Ru_1Fe_1/CoP	100(@ ~80 mV)	6(η_{20})	24.5	Ru_1Fe_1→CoP	ACS Energy Lett., 2022, 7, 1330-1337.
8	Ru_{SA+AC}/np-Mo	1000(@ 117 mV)	27(η_{10})	30.1	Mo→Ru	Chem. Eng. J., 2025, 510, 161683.
9	RuMo@MoO_x-JH	2000(@ ~250 mV)	15(η_{10})	39.9	RuMo → MoO_x	Nat. Commun., 2024, 15, 7475.
10	Ru@WO_{3-x}-W	1204(@ 200 mV)	16(η_{10})	40.7	Ru → WO_{3-x}-W	This work

References

1. X. Song, H. Yang, C. Zhang, G. Zhang, H. Wu, Y. He, M. Fu, X. Liu, S. Li and S. Wei, *Catal. Sci. Technol.*, 2024, 14, 735-745.
https://doi.org/10.1039/d3cy01485a

2. H. Yue, Z. Guo, Z. Zhou, X. Zhang, W. Guo, S. Zhen, P. Wang, K. Wang and W. Yuan, *Angew. Chem. Int. Ed.*, 2024, 63, e202409465.
https://doi.org/10.1002/anie.202409465

3.Y. Chen, Y. Liu, L. Li, T. Sakthivel, Z. Guo and Z. Dai. *Adv. Funct. Mater.*, 2024, 34, 2401452.
https://doi.org/10.1002/adfm.202401452

4. T. Zhu, J. Han, T. Sun, J. Zhao, X. Pi, J. Xu and K. Chen, *ACS Catal.*, 2024, 14, 1914-1921.

https://doi.org/10.1021/acscatal.3c04498
5. S. Liu, L. Liu, J. Liu, Y. Xiang, L. Gao, F. Fu, X. Gao and X. Jian, *ACS Appl. Nano Mater.*, 2023, 6, 22192-22201.
https://doi.org/10.1021/acsanm.3c04420
6. Y. Wang, Q. Lu, F. Li, D. Guan and Y. Bu, *Adv. Funct. Mater.*, 2023, 33, 2213523.
https://doi.org/10.1002/adfm.202213523
7. J. Li, Y. Tan, M. Zhang, W. Gou, S. Zhang, Y. Ma, J. Hu, Y. Qu, *ACS Energy Lett.*, 2022, 7, 1330-1337.
https://doi.org/10.1021/acsenergylett.1c02769
8. C. Jian, J. Yuan, T. Wang, L. Zeng and W. Liu, *Chem. Eng. J.*, 2025, 510, 161683.
https://doi.org/10.1016/j.cej.2025.161683
9. Z. Zhao, J. Sun, X. Li, S. Qin, C. Li, Z. Zhang, Z. Li and X. Meng, *Nat. Commun.*, 2024, 15, 7475.
https://doi.org/10.1038/s41467-024-51976-5

Table S3 The binding energy of Ru 3p, W 4f and O 1s of Ru@W, Ru@WO_{3-x}-W and. Ru@WO_{3-x}-W-after 100 h.

Electrodes	Ru 3p /eV		W 4f /eV			O 1s /eV	
	Ru^0	Ru^{4+}	W^{6+}	W^{5+}	W^0	OH^-	H_2O
Ru@W/TM	460.4	466.4	38.0, 35.8	33.8	31.3	530.7	532.5
Ru@WO_{3-x}-W/TM	460.3	466.2	39.0, 36.9	35.2	---	532.1	533.1
Ru@WO_{3-x}-W/TM after 100 h	460.2	466.1	38.8, 36.7	34.7	---	532.1	533.1

There are tow forms of adsorbed oxygen in the O 1s peaks of Ru@W/TM, namely OH^-(530.7 eV) and H_2O (532.5 eV). However, for the Ru@WO_{3-x}-W/TM, they are located at 532.1 and 533.1 eV. The obvious positive shift of B.E peaks of O 1s indicates the formation of $RuO(OH)_2$ phase on the surface of Ru@WO_{3-x}-W/TM. The theoretical calculation results of Karlsson et al.[28] had indicated that, after 1–6H atom is modified to the surface of RuO_2, the peak of O1s in OH will move by 1.7–2.6 eV, while the peak of O1s without H will move by 0.3–0.8 eV. For Ru@WO_{3-x}-W/TM, the O1s peak of OH^- shifts by 1.6 eV, and the O1s peak of H_2O shifts by 0.6 eV, which is basically consistent with Karlsson's calculation results. Meantime, Näslund et al.[1] had observed the same phenomenon in the O 1 s XPS spectra of RuO_2 electrode after 24 h electrolysis used for HER at a current density of 6.4 kA m^{-2} and a temperature of 90.0 °C in 8 M NaOH. This phenomenon also appeared in NP-RuO_2 prepared by electro-oxidation,[2] and its O 1s also shifted significantly. In this study, the O 1s peak in NP-RuO_2 has significantly shifted by 0.9–1.5 eV. All these can be attributed to the formation of $RuO(OH)_2$.

References

1 L.Å. Näslund, Á.S. Ingason, S. Holmin, J. Rosen, Formation of $RuO(OH)_2$ on RuO_2-based electrodes for hydrogen production, *J. Phys. Chem. C* 118 (2014) 15315 – 15323.

2 N. Cong, Y. Han, L. Tan, C. Zhai, H. Chen, J. Han, H. Fang, X. Zhou, Y. Zhu, Z. Ren, Nanoporous RuO_2 characterized by $RuO(OH)_2$ surface phase as an efficient bifunctional catalyst for overall water splitting in alkaline solution, *J. Electroanal. Chem.* 881 (2021) 114955.

Table S4 HER activities of Ru-based hydrogen spillover electrocatalyst in alkaline system

No.	Catalyst	Electrolyte	η(mV)	Tafel (mV/dec)	Hydrogen overflow path	References
1	Ru/WC_x-900	1.0 M KOH Seawater	9(η_{10}) 65(η_{100})	30 42.7	WC_x→Ru	Small, 2025, 21, 2406022.
2	Ru/ac-ZrO_2	1.0 M KOH	14(η_{10})	26.9	ZrO_2→Ru	Small, 2025, 2410436.
3	Ru/Ni $(OH)_{2-x}$	1.0 M KOH（60 ℃）	185(η_{1000})	56.95	Ru→Ni$(OH)_{2-x}$	Small, 2025, 21, 2409675.
4	Ru-Sn/SnO_2 NS	1.0 M KOH	12(η_{10})	22.7	$*OH$ Ru-Sn→SnO_2	Adv. Mater., 2024, 36, 2411942.
5	Ru/SNC	1.0 M KOH Seawater	12(η_{10}) 30(η_{10})	43.9	Ru→SNC	EES Catal., 2024, 2, 932-940.
6	RuCoP/CC	1.0 M KOH	44(η_{10})	64	Ru→Co	Angew. Chem. Int. Ed., 2024, 63, e202400069.
7	c-RP/IP HNTs	1.0 M KOH	23.2(η_{10})	30.7	Ru_2P→Ir_2P	Adv. Energy Mater., 2024, 14, 2401426.
8	Ru_1-Mo_2C	1.0 M KOH	10.8(η_{10})	38.5	Mo_2C→Ru	Energ. Environ. Sci., 2024, 17, 1397-1406.
9	Ru/Mo_2C/MoO_2	1.0 M KOH	19(η_{10})	18.3	Mo_2C/MoO_2→Ru	Adv. Mater., 2024, 36, 2410039.
10	Ru-RuSi	1.0 M KOH	27(η_{10})	27	Ru→RuSi	Angew. Chem., 2025, 137, e202423756.
11	PtRu/BNHCSs	1.0 M KOH Seawater	18(η_{10}) 190(η_{10})	37.7	Ru→Pt	Adv. Energy Mater., 2025, 15, 2405828.
12	Ru/W_2C	1.0 M KOH	17(η_{10})	17	W_2C→Ru	Adv. Energy Mater., 2025, 15, 2405546.
13	$LaCeO_x$@NGr/Ru_1	1.0 M KOH	22(η_{10})	40	$LaCeO_x$→Ru	Appl. Catal. B: Environ., 2024, 343, 123452.
14	Ru/MoO_2@NCF	1.0 M KOH 1.0 M PBS	9.2(η_{10}) 70(η_{10})	37.8 -	MoO_2→Ru	Adv. Funct. Mater., 2024, 34, 2401452.
15	5/10 ML HO^--Ru-Cu	1.0 M KOH 1.0 M PBS	9.5(η_{10}) 41(η_{10})	33 51	Ru→Cu	ACS Nano, 2023, 18, 874-884.

16	Ru/$NiMoO_{4-x}$	1.0 M KOH Seawater	206(η_{3000})	28.8	,$NiMoO_{4-x}$→Ru	Angew. Chem. Int. Ed., 2024, 63, e202316319.
17	$RuSe_{1.5}$	1.0 M KOH 1.0 M PBS	12(η_{10}) 30(η_{10})	34 --	Se→Ru	ACS Catal., 2024, 14, 1914-1921.
18	RuP/Ru@CNS	1.0 M KOH 1.0 M PBS	15(η_{10}) 80(η_{50})-	32 39	Ru→RuP	Adv. Sci., 2024, 11, 2309869.
19	Ru/Ni-NiO/$Mo_2TiC_2T_x$	1.0 M KOH 1.0 M PBS	41(η_{10}) 76(η_{10})	28 68	Ni-NiO→Ru	ACS Appl. Nano Mater., 2023, 6, 22192-22201.
20	Ru-$Ni_{0.85}Co_{0.15}Se$/NF	1.0 M KOH	18.2(η_{10})	35.61	Ru→$Ni_{0.85}Co_{0.15}Se$	J. Mater. Chem. A, 2023, 11, 7016-7024.
21	Ru-WO_{3-x}/CP	1.0 M PBS	19(η_{10})	41	WO_{3-x}→Ru	Nat. Commun., 2022, 13, 5382.
22	Ru/P-TiO_2	1.0 M KOH	27(η_{10})	28.3	Ru→P	Angew. Chem. Int. Ed., 2022, 61, e202212196.
23	Ru-$Mo_2Ti_2C_3$	1.0 M KOH	47(η_{10})	49-	Ru→$Mo_2Ti_2C_3$	J. Colloid Int. Sci., 2025, 694, 137738.
24	Ru_{SA+AC}/np-Mo	1.0 M KOH	35η_{10})	32.4	Ru→Mo	Chem. Eng. J., 2025, 510, 161683.
25	RuMo-NPCSPC	1.0 M KOH	49(η_{10})	62.3	Mo_2C→Ru	J. Colloid Int. Sci., 2025, 699, 138213.
26	Ru/F-FeCoOOH	Seawater	260(η_{2000})	106.7	Ru→F-FeCoOOH	Nano Energy, 2024, 121, 109249.
27	Ru/NC	1.0 M KOH	21.9(η_{10})	29.03	Ru^{n+}→Ru^0	Adv. Funct. Mater., 2024, 17, 2314899.
28	P-Ru-CoNi-LDH	1.0 M KOH	29(η_{10})	69	Ru→P-CoNi-LDH	Small, 2022, 18, 2104323.
29	RuC-B-O/rGO	1.0 M KOH	12(η_{10})	31.5-	Ru^{n+}→Ru^0	Angew. Chem. Int. Ed., 2025, 64, e202503871.
30	Ru@TiC	1.0 M KOH Seawater	25(η_{10}) 65(η_{100})	30.6 42.7	Ru→TiC	Small, 2025, 21, 2411975.
31	Ru/CoP	1.0 M KOH	175(η_{100})	69	Ru→CoP	Adv. Mater., 2025, 37, 2503182.
32	S_v-Ru/Ni_xS_γ	1.0 M KOH	119(η_{10})	69.79	Ru→Ni_xS_γ	Int. J. Hydrogen Energy, 2025, 139, 621-629.

References

1. J. Zhao, M. Kou, Q. Yuan, Y. Yuan and J. Zhao. *Small,* 2025, 21(1), 2406022.
https://doi.org/10.1002/smll.202406022
2. J. Niu, H. Duan, T. Sun, Z. Zhi, D. Li, X. Fan, L. Zhang and D. Yang. *Small*, 2025, 2410436.
https://doi.org/10.1002/smll.202410436
3. J. Tang, X. Liu, X. Wang, S. Wu, J. Zhu, X. Wang, T. Wang, J. Chi, Z. Wu and L. Wang. *Small*, 2025, 21(4), 2409675.
https://doi.org/10.1002/smll.202409675
4. Z.-T. Yan, S. Tao, J. Wang, X.-L. Lu and T.-B. Lu. *Adv. Mater.*, 2024, 36(46), 2411942.
https://doi.org/10.1002/adma.202411942
5. R. Tang, P. Yan, Y. Zhou and X.-Y. Yu. *EES Catalysis*, 2024, 2(4), 932-940.
https://doi.org/10.1039/d4ey00076e
6. S. Liu, Z. Li, Y. Chang, M. G. Kim, H. Jang, J. Cho, L. Hou and X. Liu. *Angew. Chem. Int. Edit.*, 2024, 63(12), e202400069.
https://doi.org/10.1002/anie.202400069
7. Y. Hong, S. Jeong, J. H. Seol, T. Kim, S. C. Cho, T. K. Lee, C. Yang, H. Baik, H. S. Park, E. Lee, S. J. Yoo, S. U. Lee and K. Lee. *Adv. Energy Mater.*, 2024, 14(29), 2401426.
https://doi.org/10.1002/aenm.202401426
8. T. Chao, W. Xie, Y. Hu, G. Yu, T. Zhao, C. Chen, Z. Zhang, X. Hong, H. Jin, D. Wang, W. Chen, X. Li, P. Hu and Y. Li. *Energ. Environ. Sci.*, 2024, 17(4), 1397-1406.
https://doi.org/10.1039/d3ee02760k
9. L. Hou, C. Li, H. Jang, M. G. Kim, J.-Z. Jiang, J. Cho, S. Liu and X. Liu. *Adv. Mater.*, 2024, 36(48), 2410039.
https://doi.org/10.1002/adma.202410039
10. L. Hou, Z. Li, H. Jang, M. G. Kim, J. Cho, W. Zhong, S. Liu and X. Liu. *Angewandte Chemie*, 2025, 137(12), e202423756.
https://doi.org/10.1002/ange.202423756
11. X. Zhao, Y. Jiang, D. Wang, Y. Zhang, M. Chen, G. Hu, H. Zhang, Z. Jin and Y. Zhou. *Adv. Energy Mater.*, 2025, 15(19), 2405828.
https://doi.org/10.1002/aenm.202405828
12. J.-Z. Jiang, S. Liu, Z. Li, M. G. Kim, H. Jang, X. Liu and L. Hou. *Adv. Energy Mater.*, 2025, 15(18), 2405546.
https://doi.org/10.1002/aenm.202405546
13. V. Dao, H. Choi, J. D. Jiménez, S. Yadava, C. Kim, T. V. Nguyen, C. Kai, P. Uthirakumara, Q. V. Le, S. D. Senanayake, H. Y. Kim and I.-H. Lee. *Appl. Catal. B: Environ.*, 2024, 343, 123452.
https://doi.org/10.1016/j.apcatb.2023.123452
14. Y. Chen, Y. Liu, L. Li, T. Sakthivel, Z. Guo and Z. Dai. *Adv. Funct. Mater.*, 2024, 34(28), 2401452.
https://doi.org/10.1002/adfm.202401452
15. Y. Liu, H. Li, X. Liu, Y. Wang, L. Wang, T. Yang, A. R. Jadhav, J. Zhang, Y. Wang, M. Wu, J. Y. Lee, M. G. Kim and H. Lee. *ACS nano*, 2023, 18(1), 874-884.
https://doi.org/10.1021/acsnano.3c09504
16. X. Liu, X. Wang, K. Li, J. Tang, J. Zhu, J. Chi, J. Lai and L. Wang. *Angew. Chem. Int. Ed.*,

2024, 63, e202316319.
https://doi.org/10.1002/anie.202316319
17. T. Zhu, J. Han, T. Sun, J. Zhao, X. Pi, J. Xu and K. Chen. *ACS Catal.*, 2024, 14(3), 1914-1921.
https://doi.org/10.1021/acscatal.3c04498
18. D. Li, R. Cai, D. Zheng, J. Ren, C.-L. Dong, Y.-C. Huang, S. J. Haigh, X. Liu, F. Gong, Y. Liu, J. Liu and D. Yang. *Adv. Sci.*, 2024, 11(22), 2309869.
https://doi.org/10.1002/advs.202309869
19. S. Liu, L. Liu, J. Liu, Y. Xiang, L. Gao, F. Fu, X. Gao and X. Jian. *ACS Appl. Nano Mater.*, 2023, 6(23), 22192-22201.
https://doi.org/10.1021/acsanm.3c04420
20. C. Mu, H. Xin, Q. Luo, Y. Li and F. Ma. *J. Mater. Chem. A*, 2023, 11(13), 7016-7024.
https://doi.org/10.1039/d3ta00600j
21. J. Chen, C. Chen, M. Qin, B. Li, B. Lin, Q. Mao, H. Yang, B. Liu and Y. Wang. *Nat. Commun.*, 2022, 13(1), 5382.
https://doi.org/10.1038/s41467-022-33007-3
22. S. Zhou, H. Jang, Q. Qin, L. Hou, M. G. Kim, S. Liu, X. Liu and J. Cho. *Angew. Chem. Int. Edit.*, 2022, 61(44), e202212196.
https://doi.org/10.1002/anie.202212196
23. X. Liu, F. Xie, Q. Xi, Y. Wang, Y. Wang, H. Li, R. Li, C. Fan, J. Liu and J. Wang. *J. Colloid Interf. Sci.*, Volume 694, 15 September 2025, 137738.
https://doi.org/10.1016/j.jcis.2025.137738
24. C. Jian, J. Yuan, T. Wang, L. Zeng and W. Liu. *Chem. Eng. J.*, Volume 510, 15 April 2025, 161683.
https://doi.org/10.1016/j.cej.2025.161683
25. D. K. Sam, Z. Tang and Y. Cao. *J. Colloid Interf. Sci.*, Volume 699, Part 2, December 2025, 138213.
https://doi.org/10.1016/j.jcis.2025.138213
26. J. Zhu, J. Chi, X. Wang, T. C., L. Guo, B. Dong, X. Liu, L. Wang. *Nano Energy*, Volume 121, March 2024, 109249.
https://doi.org/10.1016/j.nanoen.2023.109249
27. S. Zhu, Z. Li, L. Hou, M. G. Kim, H. Jang, S. Liu and X. Liu. *Adv. Funct. Mater.,* Volume34, Issue17, April 25, 2024, 2314899.
https://doi.org/10.1002/adfm.202314899
28. Q. Li, F. Huang, S. Li, H. Zhang and X. Yu. *Small*, 2022, 18(2): 2104323.
https://doi.org/10.1002/smll.202104323
29. H. Lei, W. Yang, S. Hu, L. Yi and C. Ma. *Angew. Chem. Int. Edit.*, 2025, 64, e202503871.
https://doi.org/10.1002/anie.202503871
30. J. Sun, Z. Wang, Y. Wang, Y. Song, Y. Pei, W. Yan, R. Xiong, Y. Liu, B. Lin, X. Wang, X. Zhang, J. Chen and L. Zhang. *Small*, 2025, 21(15), 2411975.
https://doi.org/10.1002/smll.202411975
31. K. Ji, S. Wang, S. Yao, Y. Ji, J. Li, X. Wang, L. Shi, G. Wang, W. Ren, J. Wang, F. Zhang, J. Xie, Z. Yang and Y. Yan. *Adv. Mater.*, 2025, 37, 2503182.
https://doi.org/10.1002/adma.202503182
32. J. Chen, J. Ni, H. Xu, X. Qian, Y. Liu, L. Jin, K. Wang, G. He and H. Chen. *Int. J. Hydrogen*

Energ., 2025, 139, 621-629.
https://doi.org/10.1016/j.ijhydene.2025.05.155